






GASP XXXIX: MeerKAT hunts Jellyfish in A2626

Tirna Deb ^{1,2}★, Marc A. W. Verheijen ¹★, Bianca M. Poggianti,³ Alessia Moretti ³, J. M. van der Hulst,¹ Benedetta Vulcani ³, Mpati Ramatsoku ^{4,5}, Paolo Serra,⁴ Julia Healy,⁶ Marco Gullieuszik,³ Cecilia Bacchini,³ Alessandro Ignesti,³ Ancla Müller,⁷ Nikki Zabel,⁸ Nicholas Lubber,^{9,10} Yara L. Jaffé¹¹ and Myriam Gitti^{12,13}

¹Kapteyn Astronomical Institute, University of Groningen, Landleven 12, NL-9747 AV Groningen, the Netherlands

²Department of Physics and Astronomy, University of the Western Cape, Robert Sobukwe Road, Bellville 7535, South Africa

³INAF – Osservatorio Astronomico di Padova, Vicolo dell’Osservatorio 5, I-35122 Padova, Italy

⁴INAF – Osservatorio Astronomico di Cagliari, Via della Scienza 5, I-09047 Selargius (CA), Italy

⁵Department of Physics and Electronics, Rhodes University, PO Box 94, Makhanda 6140, South Africa

⁶ASTRON, the Netherlands Institute for Radio Astronomy, Postbus 2, NL-7990 AA Dwingeloo, the Netherlands

⁷Faculty of Physics and Astronomy, Astronomical Institute, Ruhr University Bochum, Universitätsstr 50, D-44801 Bochum, Germany

⁸Department of Astronomy, University of Cape Town, Private Bag X3, Rondebosch 7701, South Africa

⁹Department of Physics and Astronomy, West Virginia University, PO Box 6315, Morgantown, WV 26506, USA

¹⁰Center for Gravitational Waves and Cosmology, West Virginia University, Chestnut Ridge Research Building, Morgantown, WV 26505, USA

¹¹Instituto de Física y Astronomía, Universidad de Valparaíso, Avda. Gran Bretaña 1111 Valparaíso, Chile

¹²Dipartimento di Fisica e Astronomia, Università di Bologna, via Gobetti 93/2, I-40129 Bologna, Italy

¹³INAF, Istituto di Radioastronomia di Bologna, via Gobetti 101, I-40129 Bologna, Italy

Accepted 2022 August 24. Received 2022 August 24; in original form 2021 September 27

ABSTRACT

We present MeerKAT HI observations of six jellyfish candidate galaxies (JFCGs) in the galaxy cluster, A2626. Two of the six galaxies JW100 and JW103, which were identified as JFCGs from B-band images, are confirmed as jellyfish galaxies (JFGs). Both of the JFGs have low HI content, reside in the cluster core, and move at very high velocities ($\sim 3\sigma_{cl}$). The other JFCGs, identified as non-jellyfish galaxies, are HI rich, with HI morphologies revealing warps, asymmetries, and possible tidal interactions. Both the A2626 JFGs and three other confirmed JFGs from the GASP sample show that these galaxies are HI stripped but not yet quenched. We detect HI, H α , and CO(2-1) tails of similar extent (~ 50 kpc) in JW100. Comparing the multiphase velocity channels, we do not detect any HI or CO(2-1) emission in the northern section of the tail where H α emission is present, possibly due to prolonged interaction between the stripped gas and the intracluster medium. We also observe an anticorrelation between HI and CO(2-1), which hints at an efficient conversion of HI to H₂ in the southern part of the tail. We find that both ram-pressure stripping and HI-to-H₂ conversion are significant depletion channels for atomic gas. HI-to-H₂ conversion is more efficient in the disc than in the tail.

Key words: galaxies: clusters: intracluster medium – galaxies: evolution – galaxies: ISM.

1 INTRODUCTION

In the dense cluster environment, hydrodynamical interactions such as ram-pressure stripping (RPS) between the interstellar medium (ISM) of galaxies and intracluster medium (ICM) play an important role in transforming galaxies (Gunn & Gott 1972) from star forming (SF) and gas rich, to quiescent and gas poor. ‘Jellyfish’ galaxies (JFGs) are extreme examples of RPS with ‘tentacles’ of material that stretch tens of kpc beyond their stellar discs (Smith et al. 2010; Ebeling, Stephenson & Edge 2014; Fumagalli et al. 2014). For example, one of the most studied JFG is ESO137-001 in the nearby Norma cluster, with its long, extended tail observed in multiwavelength (Sun, Donahue & Voit 2007; Jáchym et al. 2014; Fossati et al. 2016; Jáchym et al. 2019).

The extended, fragile atomic hydrogen (HI) gas discs are not only the reservoirs for star formation, but also serve as diagnostic tracers of gravitational and hydrodynamic environmental processes (Bravo-Alfaro et al. 2001; Chung et al. 2009; Jaffé et al. 2015). Images of the HI gas in galaxies show that the extended HI discs are readily affected by the cluster environment, resulting in HI stripped and HI deficient galaxies compared to field galaxies (Verheijen & Sancisi 2001; Oosterloo & van Gorkom 2005; Chung et al. 2009; Serra et al. 2013; Gogate et al. 2020; Loni et al. 2021). This deficiency and stripping is less conspicuous for the centrally concentrated and more tightly bound molecular hydrogen gas (H₂). Studies of cluster galaxies often show conflicting results that differ between clusters: low SF in HI stripped but H₂ normal galaxies (Virgo cluster, Kenney & Young 1989; Lee et al. 2017; Brown et al. 2021), and normal or slightly enhanced SF in HI deficient but H₂ rich galaxies (JFGs; Moretti et al. 2020a, b). In the Virgo cluster, some galaxies are HI deficient and show signatures of RPS, but are only moderately deficient in H₂

* E-mail: deb@astro.rug.nl (TD); verheijen@astro.rug.nl (MAWV)

(Kenney & Young 1989; Chung et al. 2009; Brown et al. 2021). In Fornax, galaxies can be H I or H₂ deficient, or deficient in both gas phases (Zabel et al. 2019; Loni et al. 2021).

Until recently, observations and studies of the environmental impact on the multiphase ISM have been limited to nearby clusters such as Virgo (Kenney & Young 1989; Chung et al. 2009; Brown et al. 2021), Fornax (Zabel et al. 2019; Loni et al. 2021), or Coma (Casoli et al. 1996; Boselli et al. 1997; Healy et al. 2021c). It is still not clear what the relative influence of the ICM pressure is on the H I and H₂ gas. It also remains a puzzle why H I stripped galaxies appear to be quiescent while the H₂ gas, which is the more direct constituent for SF, is not deficient. There are still many other questions without clear answers: How do environmental processes impact the baryon cycle in galaxies? How does SF quench in galaxies: by gas removal or consumption? Therefore, it is very timely to broaden our understanding of environmental processes acting on the multiphase ISM of galaxies in clusters. JFGs, extreme examples of RPS and often located in the dense cluster core, are excellent objects to investigate environmental effects on the multiphase ISM.

The GAs Stripping Phenomena in galaxies survey (GASP; Poggianti et al. 2017b) was carried out with the Multi Unit Spectroscopic Explorer (MUSE), observing a statistically significant sample of JFGs in nearby clusters ($z = 0.04\text{--}0.07$) over a wide range of stellar masses, morphological asymmetries, and environments. The key scientific motivation is to investigate how, where and why gas removal occurs, and to quantify the amount of star formation involved in these processes (Poggianti et al. 2017b). Within GASP, JFGs are defined as the galaxies with an H α tail at least as long as the diameter of the stellar disc. In the RPS tails of these JFGs, often *in situ* SF occurs by efficient conversion of H I to H₂ followed by the collapse of molecular clouds due to thermal instabilities, turbulent motion, etc. (Poggianti et al. 2019; Müller et al. 2021). H I gas is also ionized by the young stars that are formed *in situ* in the tail. Poggianti et al. (2017a) observed a strong correlation between RPS and the presence of an active galactic nucleus (AGN), hinting at the possibility that ram pressure is causing gas to flow towards the centre thus triggering the AGN activity. Poggianti et al. (2016) identified possible stripped galaxies as jellyfish candidates galaxies (JFCGs) purely based on B-band imaging. JO201, JO204, JO206, and JW100 were confirmed stripped galaxies i.e. JFGs with long tails by MUSE observations (Bellhouse et al. 2017, 2019; Gullieuszik et al. 2017; Poggianti et al. 2017b, 2019).

Five of the GASP JFGs (JO201, JO204, JO206, JO194, JO135) were also observed with the Jansky Very Large Array (JVLA; Perley et al. 2009) to investigate their H I gas content. Ramatsoku et al. (2019, 2020) observed that both JO201 and JO206 show a strong stripping of H I gas relative to the stellar disc (on the sky and/or in velocity). Both the H I and H α tails are of similar extent, and these galaxies have comparable H I deficiencies, with enhanced SF compared to that of galaxies of similar stellar and H I mass. However, it is worth noting that JO201 resides in a more massive and dense cluster than JO206 (Bellhouse et al. 2017, 2019; Poggianti et al. 2017b; Jaffé et al. 2018). Deb et al. (2020) observed a much longer (90 kpc) H I tail compared to the RPS H α tail (30 kpc; Gullieuszik et al. 2017) in JO204. Deb et al. (2020) also investigated whether RPS is inducing the AGN in JO204 by funnelling H I gas towards the centre of the galaxy, resulting in a redshifted H I absorption profile, but the study was inconclusive. Luber et al. (2022) investigated the H I properties of non-jellyfish galaxies in clusters with JFGs from GASP sample. Our study will add the H I picture of the of the JFCGs in A2626, and will complement the detailed studies of JW100 in other wavelengths (Poggianti et al. 2019).

Table 1. A2626 cluster properties.

Cluster properties	
RA	23:36:31 ^a
Dec.	+21:09:36.3 ^a
z	0.055292 ^b
σ_{cl}	$660 \pm 26 \text{ km s}^{-1}$ ^b
M_{200}	$3.9 \times 10^{14} M_{\odot}$ ^c
R_{200}	1.59 Mpc ^b
L_X	$1.9 \times 10^{44} \text{ erg s}^{-1}$ ^d

Note. ^aCava et al. (2009), ^bHealy et al. (2021a), ^cBiviano et al. (2017), ^dWong et al. (2008).

Healy et al. (2021b) have conducted a blind MeerKAT H I survey of the galaxy cluster A2626, which hosts six JFCGs including JW100, signifying ongoing environment driven evolution of the galaxies. In this paper, we compare the H I properties and SF of the A2626 JFCGs with other JFGs from the GASP sample residing in different clusters. In the next sections, we will first address the H I in all six JF(C)Gs and then concentrate on understanding the details of the RPS process in JW100 for which all ISM phases are now available from Poggianti et al. (2019), Moretti et al. (2020a), and our MeerKAT observations. H I observations of JW100 are the last piece of the puzzle to complete the picture of the interplay of the multiphase (atomic, molecular, ionized) ISM with itself and with the ICM.

The paper is organized as follows: Section 2 gives an overview of A2626 and the JFCGs in it. H I observations and data processing are presented in Section 3. In Section 4, we explore the H I properties of the JFCGs. In Section 5, we investigate the relation between H I deficiency and star formation rate (SFR) in the JFGs. In Section 6, we then focus on JFG JW100 and study the atomic, molecular, and ionised gas phases in different velocity channels. In Section 7, we calculate the contribution of different depletion mechanisms to the stripping of the multiphase gas in JW100. Finally in Section 8, we summarize the findings and conclusions.

Throughout this paper, we adopt a Chabrier initial mass function (IMF; Chabrier 2003), and assume a cold dark matter cosmology with $\Omega_M = 0.3$, $\Omega_{\Lambda} = 0.7$, and $H_0 = 70 \text{ km s}^{-1} \text{ Mpc}^{-1}$. At the cluster redshift ($z = 0.055292$; Healy et al. 2021a), this yields $1 \text{ arcsec} = 1.074 \text{ kpc}$.

2 A2626 AND ITS JELLYFISH CANDIDATE GALAXIES

2.1 The galaxy cluster A2626

The focus of our study is the JFCGs identified in A2626, one of 77 clusters imaged as part of the WIdE-field Nearby Galaxy-cluster Survey (WINGS; Fasano et al. 2006). A2626 is a moderately massive, X-ray emitting cluster at a redshift of $z = 0.055292$ (Healy et al. 2021a). The global properties of the cluster are listed in Table 1. It is a cooling-core cluster (Wong et al. 2008; Ignesti et al. 2018; McDonald et al. 2018; Kadam et al. 2019). The X-ray surface brightness and thermodynamic maps show cold fronts and spiral wakes, indicate sloshing and the disturbed state of the ICM of A2626 (Rizza et al. 2000; Wong et al. 2008; McDonald et al. 2018; Kadam et al. 2019). The cluster hosts a peculiar central Brightest Cluster Galaxy (BCG; IC 5338) that displays an offset nucleus in an asymmetric stellar envelope. The BCG is a radio-loud galaxy and the source of a peculiar and well-studied radio source known as ‘The Kite’ (Rizza et al. 2000; Gitti et al. 2004; Gitti 2013; Kale & Gitti 2017; Ignesti et al. 2017, 2018, 2020). Using a new spectroscopic survey, Healy et al.

Table 2. Properties of the jellyfish candidate galaxies.

Name	RA (J2000) ^a deg	Dec. (J2000) ^a deg	Optical redshifts ^{b, c}	Δcz (km s ⁻¹)	M_* ^{d, e} $\times 10^9$ M_\odot	SFR ^{c, e} M_\odot yr ⁻¹	$\pm^{c, e}$ M_\odot yr ⁻¹	$M_{\text{H I}}$ $\times 10^9$ M_\odot	\pm $\times 10^9$ M_\odot	JClass ^a
JW98	23:36:09.41	+21:11:11.8	0.0681	+3886	$5.2^{+2.6}_{-1.7}$	0.31	0.17	11	0.4	1
JW99	23:36:18.55	+21:04:04.4	0.05327	-661	$8.8^{+3.4}_{-2.5}$	2.7	0.9	24	0.5	1
JW100	23:36:25.01	+21:09:03.6	0.06189	+1978	320^{+310}_{-120}	4	0.8	2.8	1.2	5
JW101	23:37:25.92	+20:54:35.3	0.06983	+4417	16^{+7}_{-5}	4.2	1.7	8.9	0.7	1
JW102	23:35:40.01	+21:08:44.5	0.0613	+1781	$2.7^{+48}_{-2.6}$	0.3	0.18	6.5	0.3	1
JW103	23:36:26.54	+21:10:55.6	0.06189	+1876	$5.2^{+4.4}_{-2.8}$	2.2	0.9	1	0.3	2

Note. ^a Poggianti et al. (2016), ^b Healy et al. (2021a), ^c Poggianti et al. (2019), ^d Vulcani et al. (2018), ^e based on WISE, provided via private communication.

(2021a) identified six galaxy groups/substructure within and beyond the projected R_{200} radius. These substructures indicate that A2626 is actively accreting galaxies and galaxy groups from its surroundings, and confirm that A2626 is a dynamically active cosmic environment.

2.2 Jellyfish candidate galaxies in A2626

A2626 hosts six JFCGs as identified by Poggianti et al. (2016). Using WINGS B-band images to search for optical evidence of gas stripping, the JFCGs were identified based on their optical morphology. Poggianti et al. (2016) ranked the galaxies on a scale of 1 to 5, JClass = 1 being the least plausible JFG and JClass = 5 being the most plausible JFG. The six JFCGs identified in A2626 are JW98, JW99, JW100, JW101, JW102, and JW103. Their global properties are listed in Table 2 and illustrated in Fig. 1 that also indicates their projected locations in A2626. Of these galaxies, JW100 has the highest JClass = 5 and is known to be experiencing RPS of its ISM. In the top right panel of Fig. 1, JW100 clearly displays an extended RPS tail towards the South West that appears as light blue in the optical image that indicating extra-planar star formation activity, which was confirmed by MUSE observations (Poggianti et al. 2019). JW100 has been the subject of many detailed studies (as summarized below) while the other five JFCGs were not part of the GASP MUSE sample. JW103 has a low JClass = 2 and it is likely at a later stage of RPS than JW100 due to its lower stellar mass. It is at the same velocity and similar location at the cluster as JW100 with two extensions of blue light towards the West in the optical image (see top right panel of 1). The other four candidate JFGs have JClass = 1 and are least likely to be experiencing RPS (see Fig. 1).

It should be noted that JW100, JW102, and JW103 have a very similar radial velocity offset with respect to A2626 of $\Delta cz \approx +1800$ km s⁻¹ ($\sim 3\sigma_{cl}$) indicating that these galaxies are entering A2626 as a group. JW100 and JW103 with JClass > 1 are close to the X-ray emitting cluster core while JW102 is still at a substantial projected distance ($\sim 0.6 R_{200}$) and thus not strongly affected by RPS yet.

The optical morphologies of the JFCGs show a wide variety of characteristics, ranging from irregular blue systems like JW98, which Poggianti et al. (2016) suggest to be the result of harassment, to two-armed grand-design spirals with a hint of lopsidedness like JW99, to bulge-dominated like JW101. Notably, the optical image of JW100 shows some reddening of the stellar light just west of its bulge, suggesting that dust is also being removed from the disc of this galaxy. In the lower JClass galaxies, it is not always obvious which blue features hint as ongoing RPS, but their overall disturbed or lopsided optical morphologies classified these galaxies as JFCGs. The spatially resolved HI observations presented in this paper will

clarify whether these JClass = 1 galaxies are actually experiencing RPS.

Using stellar masses and SFRs determined using WISE photometry (T. Jarrett, private communication), we can compare the A2626 JFCGs to other galaxies in A2626 and different reference samples (see Section 5). The stellar masses are calculated from the 3.4 μm (W1) and 4.6 μm (W2) emission. The SFRs are determined from the PAH emission in the 12 μm (W3) band; see Cluver et al. (2014, 2017) and Jarrett et al. (2013, 2019) for details.

All the above-mentioned studies of JFCGs in A2626 lack observational information on an important constituent of the ram-pressure stripped gas, namely the H I gas, and that is what our current study contributes. H I observations of JFCGs in A2626 will provide a diverse picture of H I morphologies of such galaxies that are at different stages of stripping and can confirm whether candidate JFGs are actually experiencing ongoing RPS or not. Particularly, JW100 is one of the most well-studied JFGs so far and information about the atomic gas will complete the picture of the multiphase gas of JW100.

3 H I OBSERVATIONS AND DATA PROCESSING

A2626 was observed with the MeerKAT telescope (Jonas & MeerKAT Team 2016) as one of the first MeerKAT-64 open time observations (project code SCI-20190418-JH-01). A2626 was observed during the nights of 2019 July 15–17 for a total of 15 (3 \times 5) h. The large field-of-view of MeerKAT (61 arcmin \times 61 arcmin at a frequency of 1346 MHz where H I emission from $z = 0.055$ is detected) is adequate to cover the cluster beyond R_{200} and encompasses all the JFCGs. The sensitivity of MeerKAT enables a 3σ H I mass detection limit of $2 \times 10^8 M_\odot$ in the field centre with a linewidth of 300 km s⁻¹, and a corresponding 5σ column density of 2.5×10^{19} cm⁻² at an angular resolution of 30 arcsec. The data calibration and imaging was carried out using CARACAL (version 1.0, previously known as MeerKATHI; Józsa et al. 2020) to reduce the data and SOFI-A-2 (Serra et al. 2015) to detect the H I sources within the MeerKAT cube. For the complete details on the data calibration, imaging, and source finding, see Healy et al. (2021b).

The four low class (JClass = 1) candidate galaxies turned out to be gas rich and were identified by SOFI-A-2 [H I ID = 76 (JW98), 88 (JW99), 156 (JW101), 45 (JW102) in Healy et al. 2021b]. The atlas pages for JW98 and JW99, and JW101 and JW102 are shown in Figs 2 and 3, respectively. JW103 (JClass = 2) and JW100 (JClass = 5) were not identified by SOFI-A-2 with the general parameter settings used in Healy et al. (2021b). Both galaxies have very faint H I emission, and could only be identified visually with the knowledge of their coordinates and redshifts from optical observations. The data were smoothed using Gaussian kernels to

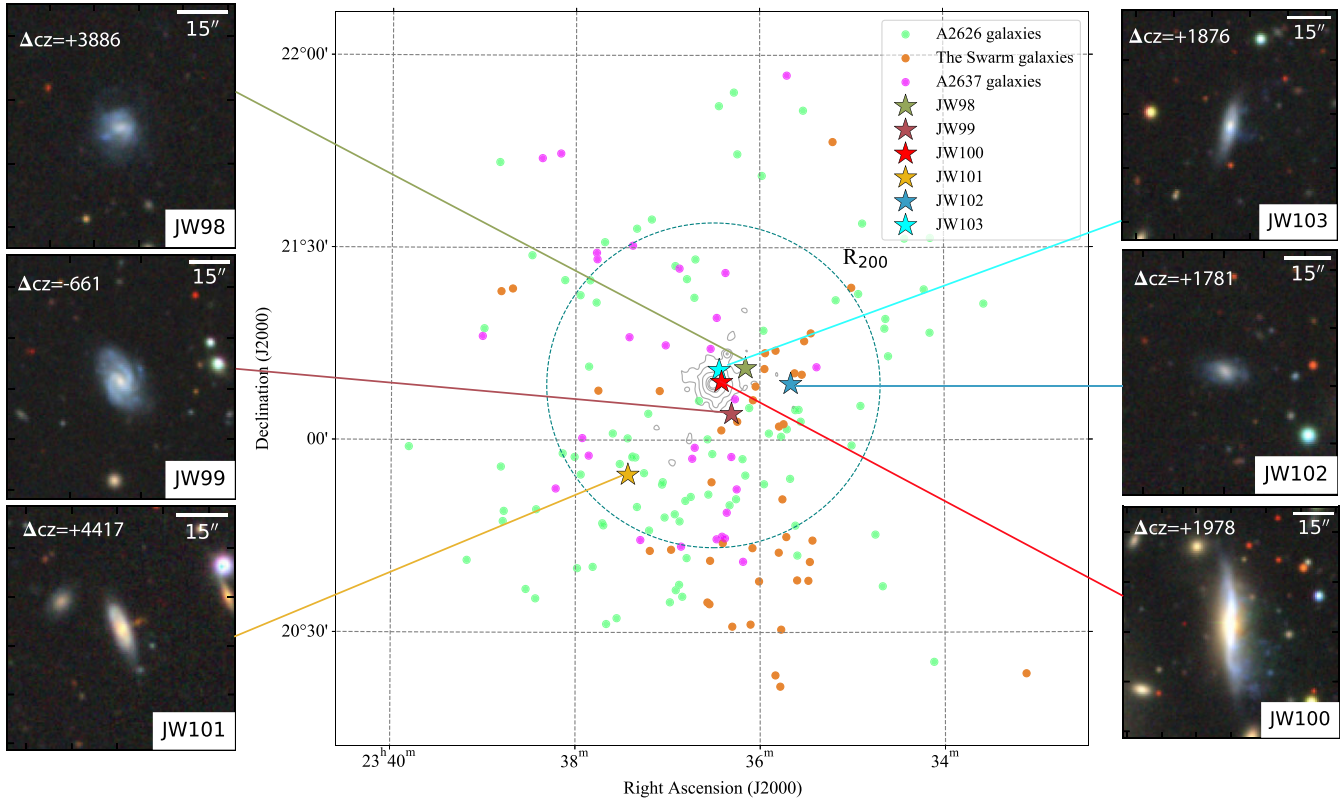


Figure 1. The location of JFCGs JW98, JW99, JW100, JW101, JW102, and JW103 in the A2626 volume (Poggianti et al. 2016). The dashed circle represents the R_{200} of A2626. The black contours represent the X-ray emission in A2626 from *ROSAT* images. The coloured dots represent the HI detections in different redshift overdensities in the A2626 volume (Healy et al. 2021a). JClass = 1 JFCGs (i.e. least probable JFGs from their optical morphologies, JW98, JW99, JW101, JW102) are outside the cluster core, higher JClass (JClass ≥ 2) galaxies JW100 and JW103 are residing close to the cluster core in projection. On the side left and right panels, we show the optical Dark Energy Camera Legacy Survey (DECaLS; Dey et al. 2019) images of JFCGs in A2626, including the Δcz velocity difference with respect to the cluster core.

angular resolutions of 15 arcsec, 20 arcsec, 25 arcsec, 30 arcsec, and with boxcar kernels to velocity resolutions of ~ 135 , ~ 225 , and $\sim 315 \text{ km s}^{-1}$ to enhance the sensitivity of the data. An angular resolution of 20 arcsec and a velocity resolution of $\sim 135 \text{ km s}^{-1}$ resulted in the highest signal-to-noise HI emission for both JW100 and JW103. Masks were constructed manually for each velocity channel containing HI emission with an HI flux of at least three times the rms noise in that channel, and visually detecting spatial coherence in the distribution of the HI emission compared to the neighbouring channels. We have then CLEAN-ed (Högbom 1974) the ‘dirty’ channels of the 20 arcsec HI datacube using the mask made, down to the 0.3σ level. The clean components were restored with a 20 arcsec circular Gaussian beam. The pixels in the cleaned 20 arcsec datacube that are outside the mask were set to zero and pixels inside the mask were summed up along the part of the frequency axis contained within the mask to obtain the total HI maps for JW100 and JW103.

4 HI PROPERTIES OF THE JELLYFISH CANDIDATE GALAXIES

The HI morphologies of the gas-rich JFCGs JW98, JW99, JW101, and JW102 do not reveal any obvious stripped jellyfish-like gas tails at the angular resolution of our MeerKAT observations (15 arcsec corresponding to 16 kpc at the redshift of A2626, see Figs 2 and 3). The detailed description of the methods used to derive the HI

properties of JW98, JW99, JW101, and JW102 can be found in Healy et al. (2021b) and the description of atlas pages of these galaxies are in Figs 2 and 3. JW98 and JW101 are at higher redshifts (see Table 2) than the redshift range of A2626 ($0.0475 < z < 0.0615$, Healy et al. 2021a) and thus are not likely members of the cluster. According to Poggianti et al. (2016), JW98 is possibly a harassed galaxy, the radio continuum shows an extension to the west which may support the harassment scenario. JW99 is a somewhat lopsided galaxy, both in the optical and in HI, and displays a mild kinematic asymmetry (see the velocity field in Fig. 2). JW101 and JW102 both seem to have warped HI discs, likely due to interactions with their neighbouring galaxies. All of these JFCGs have significant HI masses ($\sim 10^{10} M_{\odot}$), often exceeding their stellar mass.

Fig. 4 shows the HI properties of the JFGs JW100 and JW103 in the form of atlas pages. Due East of JW100, at the centre of A2626, is the peculiar, extended radio continuum source known as the ‘kite’ source. For both JW100 and JW103, the optical and HI redshifts are slightly offset (HI redshift is within the error of the optical redshift). MeerKAT HI observations of JW100 reveal a striking HI tail extending south-westwards up to ~ 20 kpc from the nucleus of the galaxy. Most of the HI emission associated with JW100 is in the tail, which is evident in the PV diagram along the tail (see Fig. 4). For JW103 the signal-to-noise of the HI emission is very low and we do not observe any HI tail in the direction of the optical tentacles that are visible in the B-band image. However, the HI emission is mostly on one side of the galaxy (north) and blue-shifted in JW103.

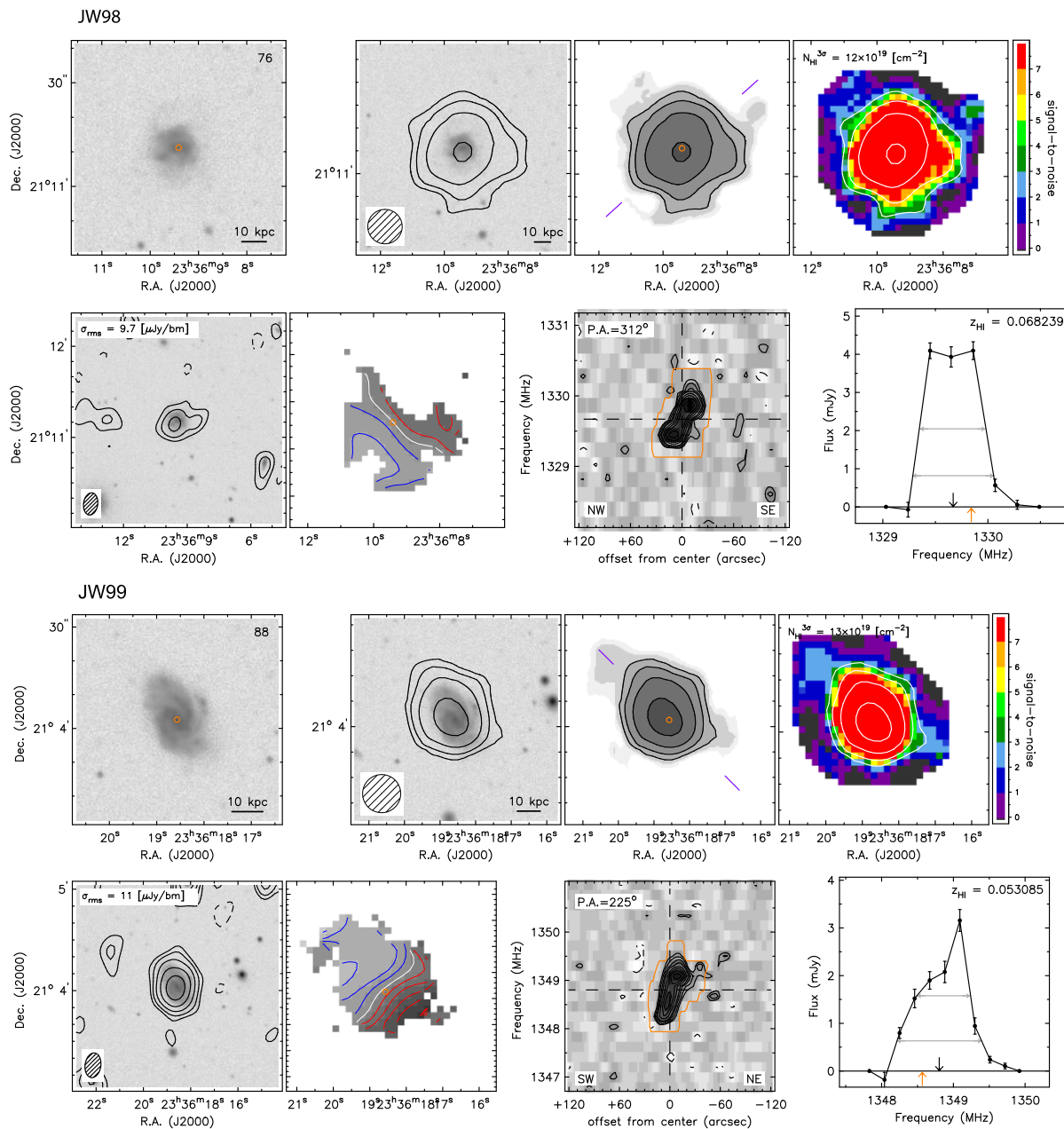


Figure 2. Atlas pages for JW98 and JW99. Clockwise from the top left panel: DECALS r-band image, the H I column density contours on DECALS g-band image in grey-scale, total H I map in grey-scale, signal-to-noise map as a colour map with the different colours representing different levels of signal-to-noise, H I global profile, H I position-velocity (PV) diagram, H I velocity field, and radio continuum map on DECALS g-band image. The H I column density contours are plotted at the levels $N_{\text{HI}}^{3\sigma} \times 2^n$ with $n = 0, 1, 2, 3, \dots$ with $N_{\text{HI}}^{3\sigma}$ the average 3σ column density for each galaxy. The H I beam size (15 arcsec) is shown in the bottom left. In the velocity field, the lighter grey-scales and blue contours show the approaching side with contour levels 25, 50, 75, 100, ..., 200 km s^{-1} . The systemic velocity v_{sys} is shown by the white contour. The darker grey-scales and red contours represent the receding side of the H I rotating disc with the contour levels $-25, -50, -75, \dots, -200 \text{ km s}^{-1}$. The radio continuum contours are plotted at the levels 2^n of the RMS noise, where $n = 0, 1, 2, 3, \dots$. Dashed contours are drawn at -2σ the RMS noise. The hatched elliptical beam in the radio continuum map is the beam size of continuum map (14.6 arcsec \times 9.30 arcsec, 171.6°). The PV diagrams are made along the major axis of the optical image, starting at the receding side of the galaxy. The position angles are mentioned on the top of each panel that are determined by visual inspection of the optical image while the receding side with respect to the systemic recession velocity of the galaxy is determined from the 3D H I datacube. The directions of the start and end points of the PV slices are indicated in the bottom left and right corners of each panel, respectively. The orange contour outlines the manually made optimum mask. The vertical dashed line indicates the optical centre of the galaxy from the SDSS. The horizontal dashed line corresponds to the central frequency as derived from the global profile. The H I spectrum and global profile of each galaxy is constructed by applying the dilated, optimum H I mask for each galaxy to the 20 arcsec resolution H I datacube. The vertical black downward arrow in the middle represents the central frequency, corresponding to the systemic velocity, which is the midpoint of the 20 per cent velocity width (W_{20}). The measured optical redshifts are shown with an orange upward arrow. The method to derive the error bars as shown on the global profile is described in section 5.1 in Healy et al. (2021b).

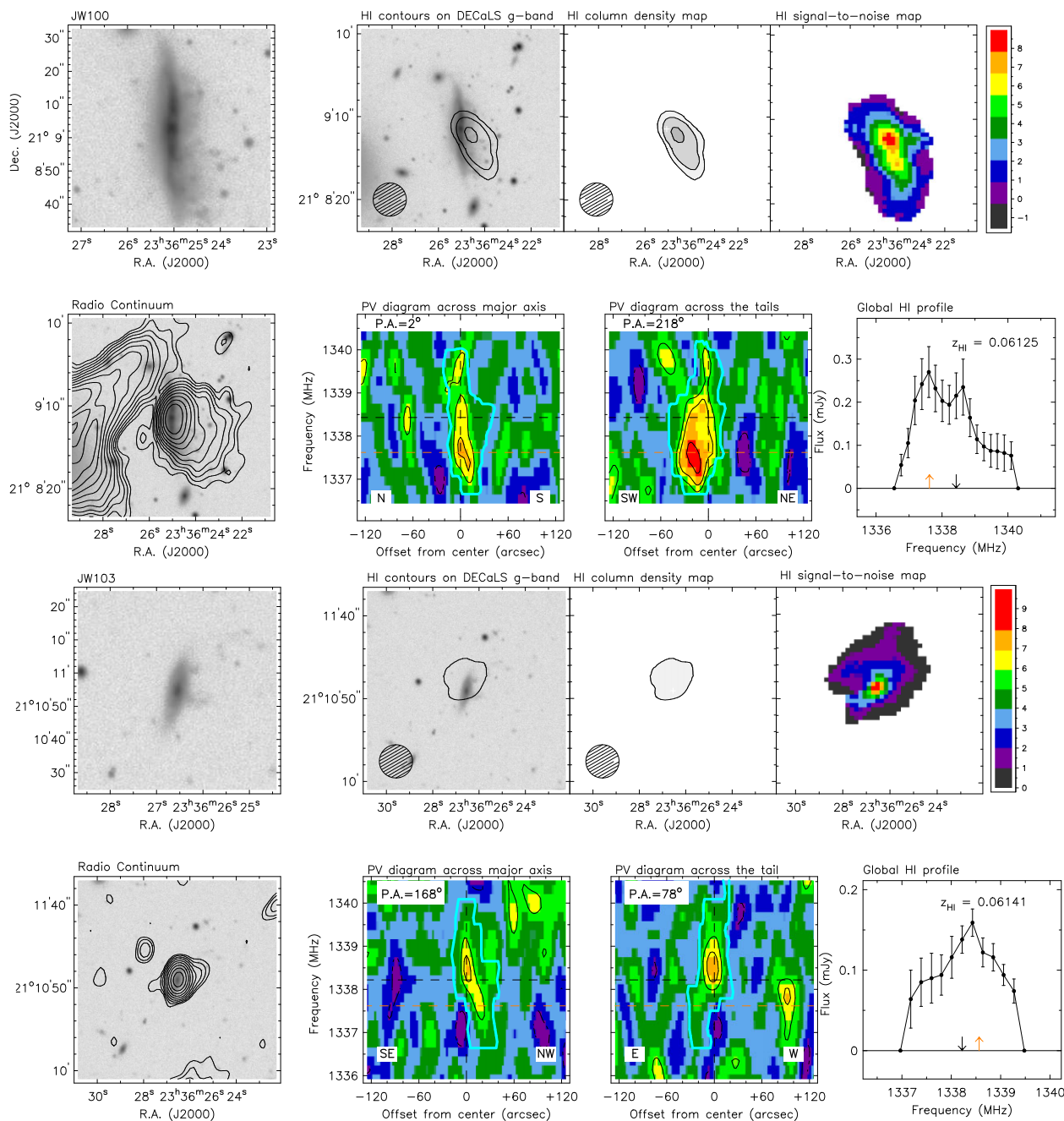


Figure 4. Atlas pages for JW100 and JW103. All the data products except the second and third panel in the bottom row are the same as in Fig. 2. The second and third panels of the second row are an H I PV diagram along the optical major axis and an H I PV diagram across the tail, respectively. The H I column density contours are plotted at the levels $N_{\text{HI}}^{3\sigma} \times 2^n$ with $n = 0, 1, 2, 3, \dots$ while $N_{\text{HI}}^{3\sigma}$, the average 3σ column density for each galaxy and the H I beam size (20 arcsec) is shown in the bottom left of the H I maps. The cyan contour in the PV diagrams outlines the manually made optimum mask as described in Section 3.

use the scaling relation from Cluver et al. (2020). Both the SFMS and quenching threshold relations in Cluver et al. (2020) are calibrated using the WISE data and the same methodologies that are used for stellar mass and SFR calculations for our sample galaxies.

We have also included the galaxies detected in the volume-limited H I surveys of the Ursa Major (UMA; Verheijen & Sancisi 2001; Busekool et al. 2021), Perseus-Pisces (PP; Bilimogga et al., in preparation), and the entire A2626 volumes as reference samples. The UMA volume is defined as a ‘supergroup’ that lacks any central

concentration while still being gravitationally bound (Wolfinger et al. 2013). At a distance of 18.6 Mpc, the volume is characterised by mostly late-type galaxies with a normal gas content (Tully & Fisher 1977). We use the H I detections from a blind H I imaging survey of the volume with the JVLA-D configuration (for more details, see Busekool et al. 2021) supplemented by targeted observations of 50 UMA galaxies (described in Verheijen & Sancisi 2001). The PP volume is a section of a ridge embedded in the PP supercluster. A blind H I imaging survey of this volume has been performed with

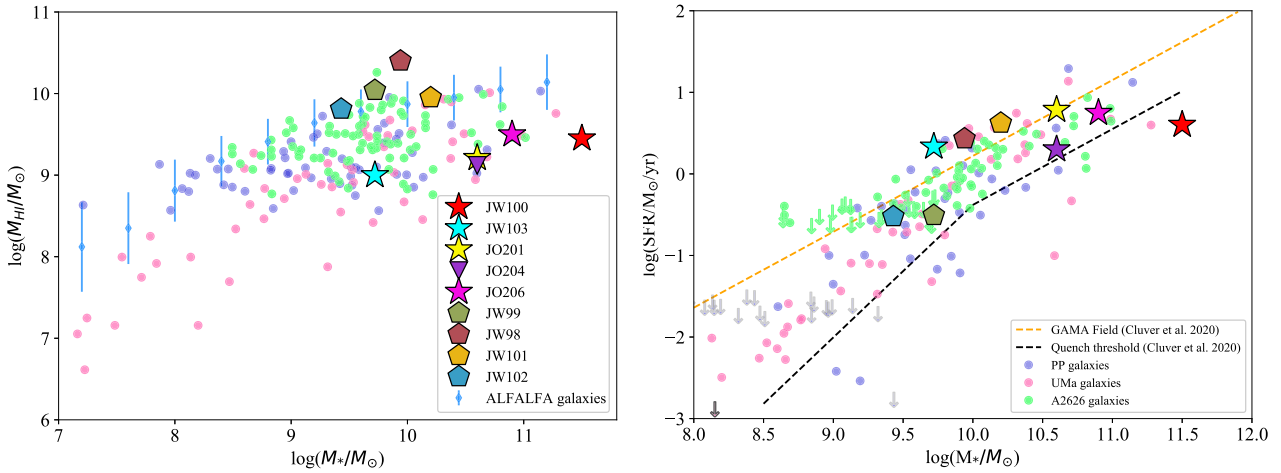


Figure 5. Left-hand panel: H I mass as a function of stellar mass for jellyfish candidate galaxies (JFGs and JFCGs) compared to reference sample galaxies. The field galaxies are the ALFALFA sample from Maddox et al. 2015, the other coloured circles are H I detected galaxies from the PP, UMa, and A2626 volumes. The star markers are identified as JFGs in our MeerKAT sample and the previous JVLAs studies of GASP galaxies (Ramatsoku et al. 2019, 2020; Deb et al. 2020). The pentagon markers are JFCGs selected from optical B-band images that are identified as non-jellyfish galaxies from their H I morphologies. Clearly, the JFGs have lower H I content compared to field galaxies or other reference sample galaxies at fixed stellar mass. Right-hand panel: SFMS for JFGs, and JFCGs. The SFMS relation and quenching threshold are taken from Cluver et al. (2020), which is calibrated using the WISE data and the same methodologies that is used for stellar mass and SFR calculations for our sample galaxies. JFGs are scattered around the SFMS. The downward arrows are 2σ upper limits on the SFR from WISE.

the JVLAs configuration (Bilimogga et al., in preparation). At a distance of 66 Mpc, the volume consists of several loose groups of galaxies that follow the large-scale structure of the PP supercluster (see Trasarti-Battistoni 1998). Since the UMa and PP observations are also volume limited H I surveys like the MeerKAT A2626 survey, we used those galaxies to compare with our JFCGs. For A2626, 97 H I sources other than JW100 and JW103 are detected in our MeerKAT observations (see Healy et al. 2021b), and they are also used in this paper as a reference sample. Stellar masses and SFRs for PP and UMa galaxies have also been calculated from WISE photometry using the same prescription as for the A2626 galaxies as mentioned in Section 2.2.

The left-hand panel of Fig. 5 shows H I versus stellar masses for the JFCGs and the reference sample galaxies. Three other H I detected JFGs namely JO201, JO204, and JO206 (Ramatsoku et al. 2019, 2020; Deb et al. 2020) from the GASP sample (Poggianti et al. 2017b) are also plotted with JW100 and JW103 in coloured star markers. Four non-stripping JFCGs are plotted with pentagon coloured star markers. Together with PP, UMa, and A2626 galaxies, we have also plotted the results from the Arcibo Legacy Fast ALFA-Sloan Digital Sky Survey (ALFALFA-SDSS) galaxy sample of field galaxies with error bars from Maddox et al. (2015), which spans a large range in stellar and H I masses. All five galaxies that are under the influence of RPS (JO201, JO204, JO206, JW100, and JW103) have relatively low H I masses for their stellar masses when compared to the reference sample galaxies (also found by Luber et al. 2022). Especially, when compared with the ALFALFA field galaxies, all five JFGs are almost 1 dex below the typical H I masses of the galaxies of similar stellar masses.

The right-hand panel of Fig. 5 shows SFR versus stellar masses for the JFGs, the reference sample galaxies and the SFMS relation. For all but JW103, the SFRs are measured with MUSE (Vulcani et al. 2018). The SFR calculations from MUSE and WISE observations are verified to be consistent (within ~ 10 per cent scatter). For JW103, we use the SFR calculated from the $12\ \mu\text{m}$ (W3) emission. Interestingly, both JFGs and JFCGs which are later identified as non-jellyfish

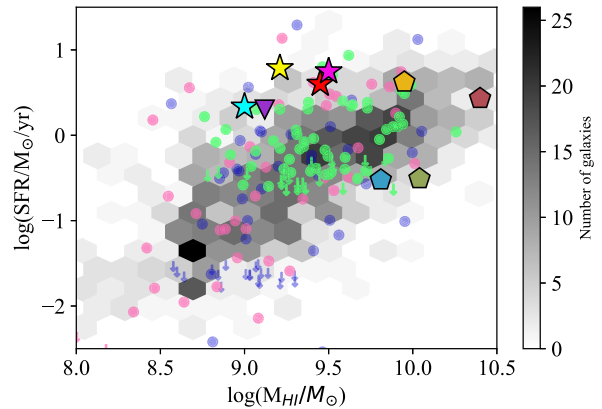


Figure 6. SFR versus H I mass for JFGs and JFCGs compared with the reference sample galaxies with the same stellar mass range. Grey hexagons are galaxies from the xGASS sample (Catinella et al. 2010) and the star, and pentagon markers represent the same JFGs and JFCGs galaxies as in Fig. 5. JFGs are H I deficient but their star formation is not quenched yet.

galaxies do not stand out with respect to the SFMS of Cluver et al. (2020), i.e. they do not necessarily have enhanced SFR compared to their stellar masses, this is contrary to what is found by Vulcani et al. (2018). However, we note that JW100 lies below the quenching threshold as defined by Cluver et al. (2020), signifying a strongly reduced star formation activity for its stellar mass.

Finally, we inspect how the atomic gas content is linked to the global star formation activity of the JFGs as compared to usual field or cluster galaxies following fig. 6 in Ramatsoku et al. (2020). We have prepared a reference sample of field galaxies with the same stellar mass range as the five JFGs ($9.7 \leq \log M_{*} \leq 11.5$) from the Extended GALEX Arcibo SDSS Survey (xGASS; Catinella et al. 2010). Fig. 6 displays SFR versus M_{HI} for the xGASS sample (Doyle & Drinkwater 2006; Huang et al. 2012; Saintonge et al. 2016) in addition to the PP, UMa, and A2626 cluster galaxies. The

coloured star and pentagon markers represent the JFGs and other JFCGs, respectively. Intriguingly, all the five JFGs lie above the distribution of the reference samples. In other words, the JFGs have higher SFRs compared to their H I masses for galaxies with similar stellar masses (Ramatsoku et al. 2019, 2020). This suggests that these galaxies are being H I stripped but are not yet quenched. Furthermore, this also implies that the little H I gas these galaxies retain, is more efficiently transformed into H₂ gas, as concluded by Moretti et al. (2020b), resulting in a high SFR for their H I masses, compared to normal galaxies of similar H I masses. Given that these JFGs are H I deficient and often do not have enhanced SFR for their M_* , they must have evolved from right to left in Fig. 6, and not so much from bottom to top. We note in the right-hand panel of Fig. 5, that the JFGs do not lie significantly above the SFMS and therefore, do not currently have an enhanced SFR for their stellar mass. Therefore, we conclude that the JFGs have not moved upwards significantly in Fig. 6. However, we cannot entirely rule out that a mild enhancement of the SFR may have occurred during a short period of time since these galaxies entered the clusters.

6 THE MULTIPHASE ISM OF JW100

6.1 Previous studies on JW100

JW100 is the proto-typical JFG. It is a nearly edge-on spiral galaxy with an AGN in its centre (Poggianti et al. 2019; Radovich et al. 2019). JW100 resides in A2626 under optimal conditions for RPS (Jaffé et al. 2018; Gullieuszik et al. 2020), with a particularly high line-of-sight velocity of 2000 km s⁻¹ with respect to the cluster rest frame and a projected distance of 83 kpc from the cluster centre (Poggianti et al. 2019). It is the most massive JFG in the entire GASP sample with a stellar mass of $3.2 \times 10^{11} M_{\odot}$ (Poggianti et al. 2019). JW100 is one of the most spectacular JFGs with extra-planar RPS tails of ionized and molecular gas, UV stellar light, X-ray, and radio continuum emission (Poggianti et al. 2019; Moretti et al. 2020a; Ignesti et al. 2022).

In the northern part of the tail, there is a lack of extra-planar clumpy CO gas and star formation while only diffuse H α is observed, with a high [O I]/H α ratio and X-ray emission. This suggests that the excess H α emission in the northern part of the tail is possibly a result of a complex ICM–ISM interplay triggered by RPS (e.g. Ferland et al. 2009; Fossati et al. 2016; Cramer et al. 2019; Campitiello et al. 2020). We note here that the northern, diffuse H α emission has a recession velocity that is inconsistent with the rotational velocity of JW100, suggesting that the ionized gas is decelerated along the orbit and longer exposed to interaction with ICM (see Section 6.2 for more details). The radio continuum emission from the tail of JW100 is mainly synchrotron emission caused by relativistic electrons ejected by supernovae explosions, indicating the presence of magnetic fields pervading the stripped gas (as in e.g. Chen et al. 2020; Müller et al. 2021; Roberts et al. 2021).

Based on ALMA observations, Moretti et al. (2020a, 2020b) found a large amount of molecular gas ($\sim 2.5 \times 10^{10} M_{\odot}$), i.e. 8 per cent of the stellar mass, a value more than an order of magnitude higher than that found in typical Virgo cluster galaxies (Corbelli et al. 2012; Brown et al. 2021) and in the local xCOLD GASS sample (Saintonge et al. 2017) for galaxies of similar stellar mass. The ALMA data reveal a 35 kpc long RPS tail of clumpy and diffuse molecular gas from the centre of JW100 (Moretti et al. 2020a). The high values of the CO line ratio ($r_{21} \geq 1$) in the southern part of the tail, the narrow, single-component CO emission lines, and low velocity dispersion hint that the tail in that region is composed of dense SF molecular

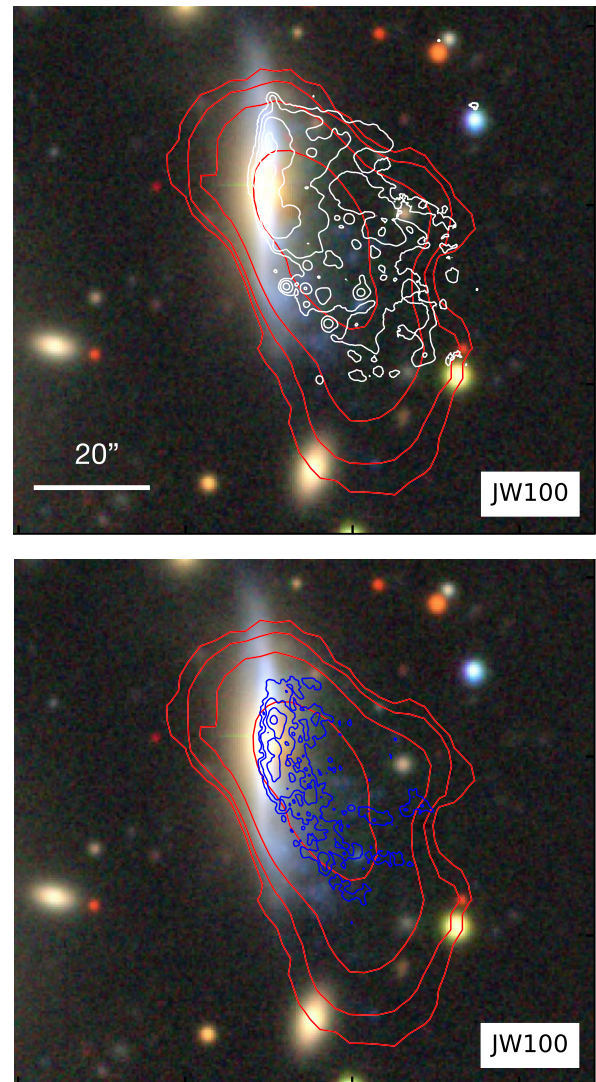


Figure 7. Multiphase gas in the RPS tail in JW100. Top panel: H α (white, 1 arcsec resolution) and H I (red, 20 arcsec resolution) contours overlaid on the DECaLS colour image. Bottom panel: CO(2-1) (blue, 1 arcsec resolution) and H I (red, 20 arcsec resolution) contours overlaid on DECaLS colour image. 1 arcsec corresponds to 1.074 kpc at a distance of JW100.

gas. This signifies that these clouds are formed *in situ*, either from the stripped H I or the diffuse molecular gas (Moretti et al. 2020a, b).

6.2 The distribution of H I in JW100 in comparison with H α and CO

Fig. 7 shows the multiphase gas in the RPS tail of JW100. The top and bottom panel of Fig. 7 show the H I emission (red, 20 arcsec resolution) on H α (white, 1 arcsec resolution) and H I emission (red, 20 arcsec resolution) on CO(2-1) (blue, 1 arcsec resolution), respectively, with the DECaLS (Dey et al. 2019) colour image in the background. The atomic, molecular, and ionized gas tails are almost of similar extent (~ 50 kpc), this small difference of the tail lengths could be also due to the different sensitivities and resolutions of the H I, H α , and CO(2-1) data.

We then inspect the distribution of gas at different recession velocities through channel maps in Fig. 8. We compare the H I

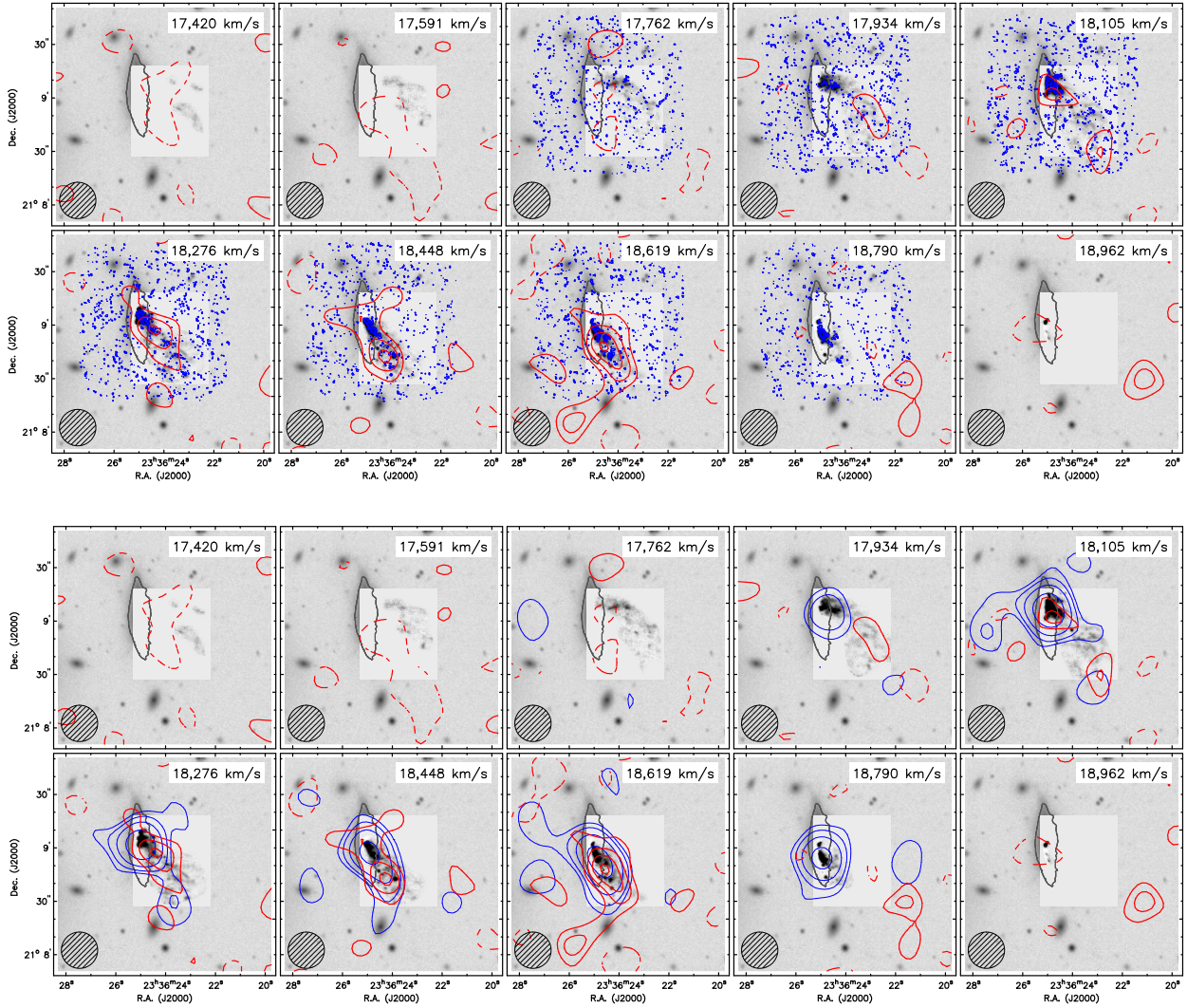


Figure 8. $H\alpha$, CO(2-1), and H I channel map overlays for JW100. In the bottom two rows, the CO(2-1) emission is smoothed to the same angular resolution as the H I emission (20 arcsec) to compare the atomic and molecular gas phases on the same spatial scales. The red solid contours represent the H I emission with contour levels of $(2, 3, 4, 5, \dots) \times \sigma$ or RMS and the dotted red contour represents the -2σ level. The blue contours indicate CO(2-1) emission with contour levels $(2, 4, 8, 16, \dots) \times \sigma$ where $\sigma = 0.28 \text{ mJy beam}^{-1}$ for the high resolution ALMA cube and $0.67 \text{ mJy beam}^{-1}$ for the 20 arcsec ALMA cube. The central light-grey rectangle represents the area in which $H\alpha$ emission is observed with MUSE, after subtraction of the [N II] emission lines and the stellar continuum emission. The image is larger than the field of view of MUSE, so the DECALS g-band image is shown in the background. The black contour represents the stellar disc and the hatched circle on the bottom left of each panel shows the size of the 20 arcsec H I beam. $H\alpha$ emission is seen in the northern part of the RPS tail but no CO(2-1) or H I emission while both $H\alpha$ and CO are anticorrelated with H I on small scales.

contours (red), CO(2-1) contours (blue), and the $H\alpha$ emission (grey-scale) at different velocities in JW100 in 10 panels. The top two rows of Fig. 8 show $H\alpha$ emission at the original MUSE angular and velocity resolution ($1 \text{ arcsec} \times 1 \text{ arcsec}$, 57.1 km s^{-1} ; Poggianti et al. 2019), CO(2-1) emission at the original ALMA resolution ($1.4 \text{ arcsec} \times 1.1 \text{ arcsec}$, 44.1 km s^{-1} ; Moretti et al. 2020a) and H I emission smoothed to 20 arcsec and $\sim 135 \text{ km s}^{-1}$. The high-resolution ALMA channel maps indicate the location of small CO(2-1) clumps. In the bottom two rows of Fig. 8, the CO(2-1) emission is also smoothed to an angular resolution of 20 arcsec to compare the atomic and molecular gas phases on the same spatial scales.

$H\alpha$ emission is visible already in the top-left panels ($17\,420$ – $17\,762 \text{ km s}^{-1}$) where H I and CO(2-1) are not yet visible. CO(2-1) and H I emission are detectable from the 4th and 5th panel, respectively.

In the 6th, 7th, and 8th panel of Fig. 8, H I emission is found further down the tail (away from the centre of JW100) than the CO(2-1) clumps. In the bottom two rows of Fig. 8, though the CO(2-1) clumps are smoothed in those panels, the centres of the CO(2-1) emission are still offset from the H I emission. The 3σ H I ‘appendix’ at the bottom left in the 8th panel, the 3σ H I peaks in the 9th and 10th panels, and the -2σ H I peaks in the 1st and 2nd panels are consistent with the noise behaviour and plausibly not associated with the H I emission or absorption of JW100. These peaks are not included in the H I mask that is used to make the H I map and the global profile.

The H I and CO(2-1) emissions in the channel maps (4–8th panel) are not exactly co-located, or anticorrelated, which suggests several possibilities. It could be because of a high rate of ionization of the H I

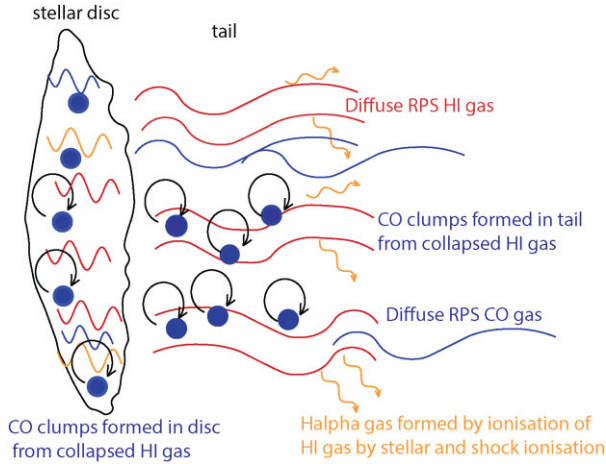


Figure 9. Cartoon of H I depletion channels. There are three principal depletion channels: RPS of the diffuse H I gas, H I to H₂ conversion in the disc and tail, and ionization of H I gas.

gas by the young massive/OB stars, or due to an efficient conversion of H I to H₂.

H α emission is extended over larger velocity range than H I and CO(2-1). The systemic velocity of JW100 is $\sim 18500 \text{ km s}^{-1}$ ($z = 0.06189$; Poggianti et al. 2019). And based on the TF relation, we would expect a rotational velocity of 400 km s^{-1} . Therefore, due to pure rotation of the galaxy, we would expect gas emission at velocities in the range of $18\,100\text{--}18\,900 \text{ km s}^{-1}$. Indeed, the channel maps show the maximum recession velocity of $18\,800 \text{ km s}^{-1}$, consistent with the rotation of the galaxy. However, the lowest velocities where the H α emission becomes visible, is roughly $17\,400 \text{ km s}^{-1}$. This difference of 1100 km s^{-1} from the systemic velocity of the galaxy cannot be accommodated by the rotation of the galaxy. Furthermore, this low recession velocity is closer to the systemic velocity of the cluster, suggesting that the H α emission is lagging behind the galaxy along its orbit through the cluster. This is observed in other GASP galaxies falling into clusters, such as JO201 in A85 (Bellhouse et al. 2017, 2019).

7 H I DEPLETION CHANNELS

In what follows, we sketch a qualitative picture of possible H I depletion channels. We estimate the relative importance of several potential H I depletion mechanisms that act on a galaxy undergoing RPS. We identify three main depletion channels for H I gas in JW100 (see schematic diagram Fig. 9). The relevance of each depletion channel depends on the amount of atomic or molecular gas that JW100 harboured before the onset of RPS (see Table 3).

We note here already that simulations suggest that up to 50 per cent of the gas can be re-accreted (Schulz & Struck 2001; Vollmer et al. 2001; Roediger, Brügggen & Hoefl 2006; Kapferer et al. 2009; Quilis, Planelles & Ricciardelli 2017; Tonnesen 2019) and gas fallback has been observed in at least one galaxy (Cramer et al. 2021). Our data do not evidence the presence of redshifted H I gas. This is not surprising, as JW100 is moving at an exceptional high velocity with respect to the cluster, which makes the gas difficult to fall back on to the galaxy. Therefore, we ignore in our calculations the gas that might be falling back to the disc.

Table 3. Expected and observed gas masses in JW100.

Gas phase	Expected mass ^a		Observed mass		
	value	range	total	disc	tail
(in units of $10^9 M_{\odot}$)					
H I	19	8.6–42 ^a	2.8	0.8	2.0
H ₂	3.5	1–10 ^b	6–25 ^c	5–24 ^c	1.9
Stellar	320				

Note. ^abased on scaling relations from Dénes, Kilborn & Koribalski (2014), ^bbased on Saintonge et al. (2017), ^cbased on Moretti et al. (2020b), the range corresponds to different values of α_{CO} varying from 0.9 (Amorín et al. 2016) to 4.3 (Bolatto, Wolfire & Leroy 2013).

7.1 Stripping (ram pressure)

One of the pivotal depletion mechanisms is RPS of the diffuse H I gas from the disc while JW100 is falling into the centre of A2626 and interacting with the hot, X-ray emitting ICM.

If we assume that the only effect of the RPS is the displacement of the initial H I gas content, then we can infer the amount of ram-pressure stripped gas based on the mass of H I gas in the tail of JW100. The mass of H I gas in the tail is derived by subtracting the amount of H I gas inside the stellar disc from the total H I gas seen in emission. The stellar disc is derived from the MUSE observations (Poggianti et al. 2019). Hence, the total H I mass in the tail is: $(2.8 \times 10^9 - 0.8 \times 10^9) M_{\odot} = 2 \times 10^9 M_{\odot}$. Thus, at least 70 per cent of the H I gas has been removed from the disc.

7.2 H I to H₂ conversion

For field galaxies in the xGASS sample (Catinella et al. 2018), depending on their stellar masses ($9.18 \leq \log M_{\star}/M_{\odot} \leq 11.2$), the H I-to-H₂ mass ratio varies in the range of 0.03–1.3. In the Fornax cluster, however, Loni et al. (2021) found $M_{\text{H}_2}/M_{\text{H I}}$ in the range of 0.1–10 for galaxies with stellar masses $9 \leq \log M_{\star}/M_{\odot} \leq 11$ (Zabel et al. 2019; Loni et al. 2021). In the case of JW100, $M_{\text{H}_2}/M_{\text{H I}}$ is 8.9, which is higher than the field galaxies in the xGASS sample, but near the high end of the $M_{\text{H}_2}/M_{\text{H I}}$ range for Fornax galaxies (Zabel et al. 2019; Moretti et al. 2020a; Loni et al. 2021). From this observation, Moretti et al. (2020b) inferred an efficient conversion of atomic to molecular gas in JW100, reinforcing the notion that H I to H₂ conversion is a significant H I depletion channel.

We aim to investigate the relative efficiency of H I-to-H₂ conversion in the disc and the tail of the JFG JW100. In Table 3, we summarize the estimated amount of H I and H₂ in the disc and the tail with the uncertainties. In the discussion that follows, we assume the maximum masses from Table 3. This may introduce some uncertainty in the final calculation, but the overall conclusion of our considerations remains unaffected.

7.2.1 H I to H₂ conversion in the disc

The current amount of H I in the disc is an order of magnitude less than the expected amount of H I with which the galaxy entered into the cluster (see Table 3). The missing H I in the disc is either stripped from the disc or locally converted into H₂. However, the amount of H₂ in the disc is roughly a factor 5 larger than the estimated amount of H₂ before the onset of RPS. The amount of H₂ gas that the disc gained is: observed H₂ mass in the disc minus expected H₂ mass which results in $14 \times 10^9 M_{\odot}$. Therefore, the excess of H₂ in the disc might have formed from H I that was present in the disc before

the onset of RPS. Thus, if all the H_2 in the disc is formed from $H\text{I}$ gas then ($14/42 \Rightarrow$) $1/3$ of $H\text{I}$ is converted into H_2 in the disc.

7.2.2 $H\text{I}$ to H_2 conversion in the tail

A significant fraction of the $H\text{I}$ gas in the disc is pushed out into the tail where it can also be converted into H_2 . Interestingly, combining LOFAR, MeerKAT, and JVLA radio continuum observations of JW100, Ignesti et al. (2022) estimated the strength of the magnetic field that could be strong enough to shield the stripped ISM gas from the ICM (Müller et al. 2021). The draping of the magnetized plasma around the tail is possibly preventing thermal conduction and hydrodynamic turbulence by the hot ICM, enabling the stripped $H\text{I}$ gas to cool and condense into molecular clumps (e.g. Sparre, Pfrommer & Ehlert 2020; Ge et al. 2021; Müller et al. 2021). The fact that we observe ongoing star formation associated with these clumps suggests that these clumps fragment further into giant molecular clouds (Poggianti et al. 2019; Moretti et al. 2020b).

Following the calculation in the previous subsection, the $H\text{I}$ gas that is pushed out of the disc into the tail, eventually into the ICM is: expected amount of $H\text{I}$ mass minus the amount of $H\text{I}$ in the disc minus the amount of $H\text{I}$ converted into H_2 in the disc which results in $27 \times 10^9 M_\odot$. Thus, by assuming that H_2 in the tail is formed from $H\text{I}$, we infer that $1.9/27 \sim 7$ percent of the diffuse $H\text{I}$ gas is converted into H_2 gas in the tail. In the previous subsection, we concluded that $1/3$ of the $H\text{I}$ is locally converted into H_2 . Hence, the conversion of $H\text{I}$ into H_2 in the disc is several times more efficient than in the tail. Thus, $30 + 7 = 37$ percent of the $H\text{I}$ is converted into H_2 and 60 percent is blown out of the galaxy.

7.2.3 H_2 versus $H\text{I}$ ratio map

We have calculated the spatially resolved atomic to molecular gas fraction for both the disc and the tail. The relative amounts of both $H\text{I}$ and H_2 in the disc and the tail are based on the stellar disc defined by the MUSE observations (Poggianti et al. 2019; Moretti et al. 2020a). The bottom panel in Fig. 10 presents the ratio map of H_2 versus $H\text{I}$ surface mass density (both measured in units of M_\odot/pc^2). The map is constructed by smoothing the $H\text{I}$ and H_2 column density maps to 20 arcsec resolution and regriding the maps to the same pixel sizes (0.2 arcsec). Though we are limited by the resolution of the $H\text{I}$ data, evidently, there is a negative gradient along the tail, implying there is more $H\text{I}$ compared to H_2 towards the tip of the tail.

7.3 $H\text{I}$ to $H\alpha$ conversion

Ionization of $H\text{I}$ owing to radiation from young stars or shock ionization is another depletion channel for $H\text{I}$ gas. We have investigated the spatially resolved ionized to atomic gas fraction for both the disc and the tail of JW100 using the same strategy we used for the molecular to atomic gas fraction. The top panel in Fig. 10 shows the ratio map for $H\alpha$ versus $H\text{I}$ surface mass density (surface mass density is measured in units of M_\odot/pc^2 and $H\alpha$ emissivity in $\text{erg s}^{-1} \text{cm}^{-2} \text{pc}^{-2}$) for JW100. In this case also, there is a gradient along the tail, implying that the ionization efficiency of neutral gas is decreasing along the tail. The lower limit of $H\alpha$ gas estimated from the MUSE observations is $4.6 \times 10^6 M_\odot$. Thus, we note that the $H\text{I}$ mass in the tail is an order of magnitude more than the ionized gas mass from which we infer that the ionization of neutral gas plays a minor role in the depletion of the neutral atomic gas.

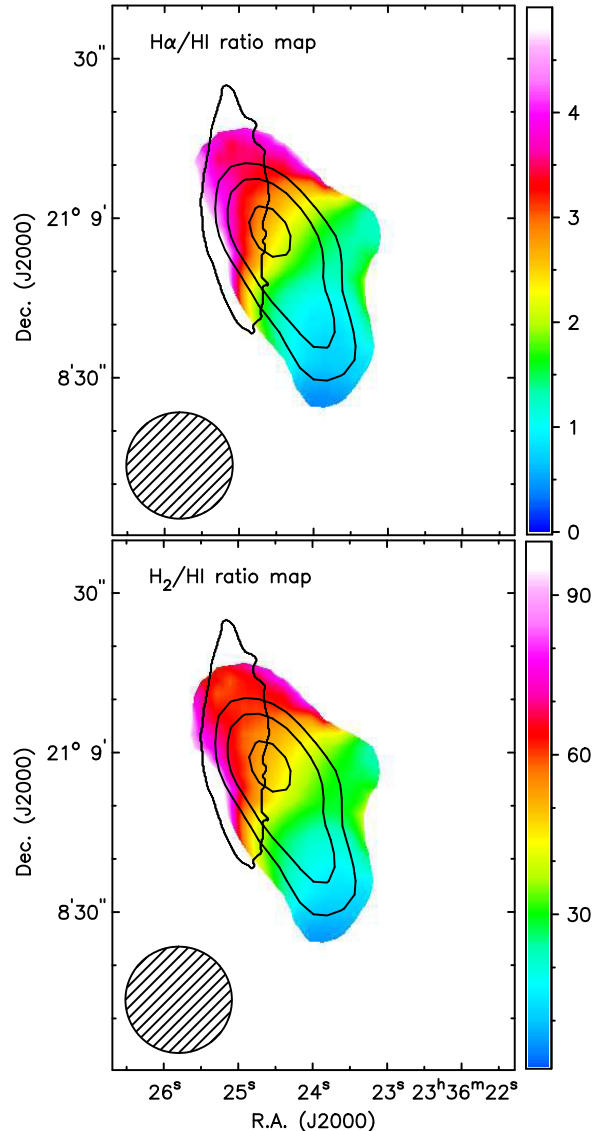


Figure 10. $H\alpha/H\text{I}$ and $H_2/H\text{I}$ ratio maps of JW100. The maps are constructed by smoothing the $H\text{I}$, H_2 , and $H\alpha$ column density maps to 20 arcsec resolution and regriding the maps to the same pixel sizes (0.2 arcsec). The black curved contour inside represents the stellar disc. The black solid contours represent the $H\text{I}$ emission with contour levels (3, 4, 5,...) $\times \sigma$ or RMS. We limit the ratio map to within the 1 sigma contour of the $H\text{I}$ column density map. The beam size is shown in the bottom left. The negative gradient in both the maps shows that there is an abundance of $H\text{I}$ over H_2 or $H\alpha$ along the extended tail. Considering the MeerKAT beam size, we note that there are only 2–3 resolution elements in these ratio maps.

8 SUMMARY

In this work, we have presented MeerKAT $H\text{I}$ observations of the JFCGs in the A2626 galaxy cluster. Among the six JFCGs as identified by Poggianti et al. (2016) from their optical morphologies in WINGS B-band images, only JW100 is identified as a JFG from its optical and $H\text{I}$ morphologies. JW103 is probably a ram-pressure stripped galaxy at a later stage of stripping. Both JW100 and JW103 are moving at a very high similar velocity ($cz \sim +1800 \text{ km s}^{-1}$, $\sim 3\sigma_{cl}$) with respect to the ICM of A2626, suggesting that these galaxies are entering as a group, confirmed by Healy et al. (2021a).

Both of these galaxies reside close to the X-ray emitting cluster core, thus in the most favourable conditions for RPS. In our upcoming work, taking advantage of these MeerKAT HI observations, we expect to identify more RPS galaxies in the A2626 volume that could not be identified from their optical morphologies.

- The four JFCGs namely JW98, JW99, JW101, JW102 have significant HI masses ($\sim 10^{10} M_{\odot}$). Their HI imaging reveals warps, morphological and kinematic asymmetries, possible tidal interactions and no convincing signature of RPS.

- JW103 is barely detected in HI and very HI deficient ($M_{\text{HI}} = 10^9 M_{\odot}$). While in the optical image of JW103, we observe blue tentacles towards the west, we do not detect any HI tails in the direction of the optical tail, possibly because the HI emission is below the detection limit. Interestingly, we see a radio continuum tail in the direction of the optical tail, which is possibly due to advection of relativistic electrons by the ram pressure wind (Ignesti et al. 2022).

- We investigated HI versus stellar masses for JFCGs compared to a reference sample of galaxies from the PP, UMa, A2626, and ALFALFA surveys of field galaxies (Maddox et al. 2015). All JFCGs have lower HI masses for their stellar masses compared to most field or cluster galaxies while other JFCGs are HI rich. We then plotted SFR versus stellar masses for the JFCGs, the reference sample galaxies and the SFMS relations. None of the JFCGs and previously studied GASP JFCGs stand out with respect to the SFMS of Cluver et al. (2020).

- Finally, when we compared the HI content versus the SFR in the JFCGs and the reference sample, all five JFCGs stand out in the relation because of the lower HI masses for their SFRs. It means that these galaxies are HI stripped but not yet quenched.

- HI observations of JW100 reveal an extended HI tail towards the south-west up to ~ 50 kpc from the stellar body of the galaxy. Comparing the H α , CO(2-1), and HI channel maps in JW100, we detect H α emission in the northern part of the RPS tail with no CO(2-1) or HI counterpart (but where X-ray emission is present; Poggianti et al. 2019) possibly because of complex ISM-ICM interaction due to prolonged RPS. Moreover, both H α and CO are anticorrelated with HI, hinting at an efficient conversion of HI to H₂ in the tail. We hypothesize that the draping of the magnetic plasma around the tail is preventing thermal conduction and hydrodynamic turbulence by the hot ICM, enabling the stripped HI gas to cool and condense into H₂ clumps (e.g. Müller et al. 2021).

- The spatially resolved H α /HI and H₂/HI ratio maps of JW100 show a gradient along the tail, implying there is more HI compared to H₂ or H α towards the tip of the extended tail. We estimated the relative importance of the different depletion mechanisms of the HI gas in JW100 and we identify three main depletion channels: RPS removal, conversion of HI to H₂, and ionization of the HI. We found that both RPS and HI-to-H₂ conversion are significant depletion channels. HI-to-H₂ conversion is more efficient in the disc than in the tail.

ACKNOWLEDGEMENTS

We thank Tom Jarrett for kindly providing the SFRs and stellar masses for the A2626, PP, and UMa galaxies from WISE observations. TD thanks Pooja Bilimogga for providing HI data on PP and UMa galaxies. This paper makes use of the MeerKAT data (Project ID: SCI-20190418-JH-01). The MeerKAT telescope is operated by the South African Radio Astronomy Observatory, which is a facility of the National Research Foundation, an agency of the Department of Science and Innovation. MV acknowledges the Netherlands Foundation for Scientific Research support through VICI grant

016.130.338 and the Leids Kerkhoven-Bosscha Fonds (LKBF) for travel support. Based on observations collected at the European Organization for Astronomical Research in the Southern Hemisphere under ESO programme 196.B-0578, this project has received funding from the European Research Council (ERC) under the European Union's Horizon 2020 research and innovation programme (grant agreement No. 833824). JMvdH acknowledges support from the European Research Council under the European Union's Seventh Framework Programme (FP/2007-2013)/ERC Grant Agreement nr. 291531. JH has received funding from the European Research Council (ERC) under the European Union's Horizon 2020 research and innovation programme (grant agreement No. 882793/MeerGas). AI acknowledges the Italian PRIN-Miur 2017 (PI A. Cimatti). YJ acknowledges financial support from CONICYT PAI (Concurso Nacional de Insercion en la Academia 2017) No. 79170132 and FONDECYT Iniciacion 2018 No. 11180558.

DATA AVAILABILITY

The data underlying this article will be shared on reasonable request to the corresponding author.

REFERENCES

- Amorín R., Muñoz-Tuñón C., Aguerrí J. A. L., Planesas P., 2016, *A&A*, 588, A23
- Bellhouse C. et al., 2017, *ApJ*, 844, 49
- Bellhouse C. et al., 2019, *MNRAS*, 485, 1157
- Biviano A. et al., 2017, *A&A*, 607, A81
- Bolatto A. D., Wolfire M., Leroy A. K., 2013, *ARA&A*, 51, 207
- Boselli A., Gavazzi G., Lequeux J., Buat V., Casoli F., Dickey J., Donas J., 1997, *A&A*, 327, 522
- Bravo-Alfaro H., Cayatte V., van Gorkom J. H., Balkowski C., 2001, *A&A*, 379, 347
- Brinchmann J., Charlot S., White S. D. M., Tremonti C., Kauffmann G., Heckman T., Brinkmann J., 2004, *MNRAS*, 351, 1151
- Brown T. et al., 2021, *ApJS*, 257, 21
- Busekool E., Verheijen M. A. W., van der Hulst J. M., Tully R. B., Trentham N., Zwaan M. A., 2021, *MNRAS*, 501, 2608
- Campitiello S., Celotti A., Ghisellini G., Sbarro T., 2020, *A&A*, 640, A39
- Casoli F., Dickey J., Kazes I., Boselli A., Gavazzi G., Jore K., 1996, *A&AS*, 116, 193
- Catinella B. et al., 2010, *MNRAS*, 403, 683
- Catinella B. et al., 2018, *MNRAS*, 476, 875
- Cava A. et al., 2009, *A&A*, 495, 707
- Chabrier G., 2003, *PASP*, 115, 763
- Chen H. et al., 2020, *MNRAS*, 496, 4654
- Chung A., van Gorkom J. H., Kenney J. D. P., Crowl H., Vollmer B., 2009, *AJ*, 138, 1741
- Cluver M. E. et al., 2014, *ApJ*, 782, 90
- Cluver M. E., Jarrett T. H., Dale D. A., Smith J. D. T., August T., Brown M. J. I., 2017, *ApJ*, 850, 68
- Cluver M. E. et al., 2020, *ApJ*, 898, 20
- Corbelli E. et al., 2012, *A&A*, 542, A32
- Cramer W. J., Kenney J. D. P., Sun M., Crowl H., Yagi M., Jáchym P., Roediger E., Waldron W., 2019, *ApJ*, 870, 63
- Cramer W. J. et al., 2021, *ApJ*, 921, 22
- Deb T. et al., 2020, *MNRAS*, 494, 5029
- Dénes H., Kilborn V. A., Koribalski B. S., 2014, *MNRAS*, 444, 667
- Dey A. et al., 2019, *AJ*, 157, 168
- Doyle M. T., Drinkwater M. J., 2006, *MNRAS*, 372, 977
- Ebeling H., Stephenson L. N., Edge A. C., 2014, *ApJ*, 781, L40
- Elbaz D. et al., 2007, *A&A*, 468, 33
- Fasano G. et al., 2006, *A&A*, 445, 805

- Ferland G. J., Fabian A. C., Hatch N. A., Johnstone R. M., Porter R. L., van Hoof P. A. M., Williams R. J. R., 2009, *MNRAS*, 392, 1475
- Fossati M., Fumagalli M., Boselli A., Gavazzi G., Sun M., Wilman D. J., 2016, *MNRAS*, 455, 2028
- Fumagalli M., Fossati M., Hau G. K. T., Gavazzi G., Bower R., Sun M., Boselli A., 2014, *MNRAS*, 445, 4335
- Ge C. et al., 2021, *MNRAS*, 505, 4702
- Gitti M., 2013, *MNRAS*, 436, L84
- Gitti M., Brunetti G., Ferretti L., Setti G., 2004, *A&A*, 417, 1
- Gogate A. R., Verheijen M. A. W., Deshev B. Z., van Gorkom J. H., Montero-Castaño M., Hulst J. M. v. d., Jaffé Y. L., Poggianti B. M., 2020, *MNRAS*, 496, 3531
- Gullieuszik M. et al., 2017, *ApJ*, 846, 27
- Gullieuszik M. et al., 2020, *ApJ*, 899, 13
- Gunn J. E., Gott J. R. III, 1972, *ApJ*, 176, 1
- Healy J., Willner S. P., Verheijen M. A. W., Blyth S. L., 2021a, preprint ([arXiv:2106.08806](https://arxiv.org/abs/2106.08806))
- Healy J., Deb T., Verheijen M. A. W., Blyth S.-L., Serra P., Ramatsoku M., Vulcani B., 2021b, preprint ([arXiv:2106.13018](https://arxiv.org/abs/2106.13018))
- Healy J. et al., 2021c, *A&A*, 650, A76
- Högbom J. A., 1974, *A&AS*, 15, 417
- Huang S., Haynes M. P., Giovanelli R., Brinchmann J., 2012, *ApJ*, 756, 113
- Ignesti A., Gitti M., Brunetti G., Ferretti L., Giovannini G., 2017, *A&A*, 604, A21
- Ignesti A., Gitti M., Brunetti G., O'Sullivan E., Sarazin C., Wong K., 2018, *A&A*, 610, 89
- Ignesti A. et al., 2020, *A&A*, 643, A172
- Ignesti A. et al., 2022, *ApJ*, 924, 64
- Jáchym P., Combes F., Cortese L., Sun M., Kenney J. D. P., 2014, *ApJ*, 792, 11
- Jáchym P. et al., 2019, *ApJ*, 883, 145
- Jaffé Y. L., Smith R., Candlish G. N., Poggianti B. M., Sheen Y.-K., Verheijen M. A. W., 2015, *MNRAS*, 448, 1715
- Jaffé Y. L. et al., 2018, *MNRAS*, 476, 4753
- Jarrett T. H. et al., 2013, *AJ*, 145, 6
- Jarrett T. H., Cluver M. E., Brown M. J. I., Dale D. A., Tsai C. W., Masci F., 2019, *ApJS*, 245, 25
- Jonas J. L., MeerKAT Team, 2016, in Taylor R., Camilo F., Leeuw L., Moodley K., eds, *MeerKAT Science: On the Pathway to the SKA. Proceedings of Science, Stellenbosch*, p. 1
- Józsa G. I. G. et al., 2020, in Pizzo R., Deul E. R., Mol J. D., Plaa J. D., Verkouter H., eds, *ASP Conf. Ser. Vol. 527, Astronomical Data Analysis Software and Systems XXIX. Astron. Soc. Pac., San Francisco*, p. 635
- Kadam S. K., Sonkamble S. S., Pawar P. K., Patil M. K., 2019, *MNRAS*, 484, 4113
- Kale R., Gitti M., 2017, *MNRAS*, 466, L19
- Kapferer W., Sluka C., Schindler S., Ferrari C., Ziegler B., 2009, *A&A*, 499, 87
- Kenney J. D. P., Young J. S., 1989, *ApJ*, 344, 171
- Lee B. et al., 2017, *MNRAS*, 466, 1382
- Loni A. et al., 2021, *A&A*, 648, A31
- Luber N. et al., 2022, *ApJ*, 927, 39
- McDonald M., Gaspari M., McNamara B. R., Tremblay G. R., 2018, *ApJ*, 858, 45
- Maddox N., Hess K. M., Obreschkow D., Jarvis M. J., Blyth S. L., 2015, *MNRAS*, 447, 1610
- Moretti A. et al., 2020a, *ApJ*, 889, 9
- Moretti A. et al., 2020b, *ApJ*, 897, L30
- Müller A. et al., 2021, *Nat. Astron.*, 5, 159
- Noeske K. G. et al., 2007, *ApJ*, 660, L43
- Oosterloo T., van Gorkom J., 2005, *A&A*, 437, L19
- Perley R. et al., 2009, *Proc. IEEE*, 97, 1448
- Poggianti B. M. et al., 2016, *AJ*, 151, 78
- Poggianti B. M. et al., 2017a, *Nature*, 548, 304
- Poggianti B. M. et al., 2017b, *ApJ*, 844, 48
- Poggianti B. M. et al., 2019, *ApJ*, 887, 155
- Quilis V., Planelles S., Ricciardelli E., 2017, *MNRAS*, 469, 80
- Radovich M., Poggianti B., Jaffé Y. L., Moretti A., Bettoni D., Gullieuszik M., Vulcani B., Fritz J., 2019, *MNRAS*, 486, 486
- Ramatsoku M. et al., 2019, *MNRAS*, 487, 4580
- Ramatsoku M. et al., 2020, *A&A*, 640, A22
- Rizza E., Loken C., Bliton M., Roettiger K., Burns J. O., Owen F. N., 2000, *AJ*, 119, 21
- Roberts I. D. et al., 2021, *A&A*, 650, A111
- Roediger E., Brüggem M., Hoeft M., 2006, *MNRAS*, 371, 609
- Saintonge A. et al., 2016, *MNRAS*, 462, 1749
- Saintonge A. et al., 2017, *ApJS*, 233, 22
- Schulz S., Struck C., 2001, *MNRAS*, 328, 185
- Serra P. et al., 2013, *MNRAS*, 428, 370
- Serra P. et al., 2015, *MNRAS*, 448, 1922
- Smith R. J. et al., 2010, *MNRAS*, 408, 1417
- Sparre M., Pfrommer C., Ehlert K., 2020, *MNRAS*, 499, 4261
- Speagle J. S., Steinhardt C. L., Capak P. L., Silverman J. D., 2014, *ApJS*, 214, 15
- Sun M., Donahue M., Voit G. M., 2007, *ApJ*, 671, 190
- Tomczak A. R. et al., 2016, *ApJ*, 817, 118
- Tonnesen S., 2019, *ApJ*, 874, 161
- Trasarti-Battistoni R., 1998, *A&AS*, 130, 341
- Tully R. B., Fisher J. R., 1977, *A&A*, 500, 105
- Verheijen M. A. W., Sancisi R., 2001, *A&A*, 370, 765
- Vollmer B., Cayatte V., Balkowski C., Duschl W. J., 2001, *ApJ*, 561, 708
- Vulcani B. et al., 2018, *ApJ*, 866, L25
- Wolfinger K., Kilborn V. A., Koribalski B. S., Minchin R. F., Boyce P. J., Disney M. J., Lang R. H., Jordan C. A., 2013, *MNRAS*, 428, 1790
- Wong K.-W., Sarazin C. L., Blanton E. L., Reiprich T. H., 2008, *ApJ*, 682, 155
- Zabel N. et al., 2019, *MNRAS*, 483, 2251

This paper has been typeset from a $\text{\TeX}/\text{\LaTeX}$ file prepared by the author.